The Astrophysical Journal, 779:20 (6pp), 2013 December 10 doi:10.1088/0004-637X/779/1/20

SPIN–ORBIT COUPLING AND CHAOTIC ROTATION FOR COORBITAL BODIES IN QUASI-CIRCULAR ORBITS

Alexandre C. M. Correia[1,2] and Philippe Robutel[2]
[1] Departamento de Física, I3N, Universidade de Aveiro, Campus de Santiago, 3810-193 Aveiro, Portugal
[2] Astronomie et Systèmes Dynamiques, IMCCE-CNRS UMR8028, 77 Av. Denfert-Rochereau, F-75014 Paris, France
Received 2013 August 15; accepted 2013 September 3; published 2013 November 22

ABSTRACT

Coorbital bodies are observed around the Sun sharing their orbits with the planets, but also in some pairs of satellites around Saturn. The existence of coorbital planets around other stars has also been proposed. For close-in planets and satellites, the rotation slowly evolves due to dissipative tidal effects until some kind of equilibrium is reached. When the orbits are nearly circular, the rotation period is believed to always end synchronous with the orbital period. Here we demonstrate that for coorbital bodies in quasi-circular orbits, stable non-synchronous rotation is possible for a wide range of mass ratios and body shapes. We show the existence of an entirely new family of spin–orbit resonances at the frequencies $n \pm k\nu/2$, where n is the orbital mean motion, ν the orbital libration frequency, and k an integer. In addition, when the natural rotational libration frequency due to the axial asymmetry, σ, has the same magnitude as ν, the rotation becomes chaotic. Saturn coorbital satellites are synchronous since $\nu \ll \sigma$, but coorbital exoplanets may present non-synchronous or chaotic rotation. Our results prove that the spin dynamics of a body cannot be dissociated from its orbital environment. We further anticipate that a similar mechanism may affect the rotation of bodies in any mean-motion resonance.

Key words: celestial mechanics – planetary systems – planets and satellites: general

Online-only material: color figures

1. INTRODUCTION

Coorbital bodies have fascinated astronomers and mathematicians since Lagrange (1772) found an equilibrium configuration where three bodies are located at the vertices of an equilateral triangle. Gascheau (1843) proved that for a circular motion of the three bodies, the Lagrange equilibrium points were stable under specific conditions fulfilled by the three masses. In 1906, the first object of this kind was observed (Wolf 1906), the asteroid Achilles, that shares its orbit with Jupiter around the Sun, leading on average by 60°. At present, more than 4000 coorbital bodies are known in the solar system,[3] sharing their orbits with the planets. More interestingly, pairs of tidally evolved coorbital satellites were also observed around Saturn in a wide variety of orbital configurations (e.g., Robutel et al. 2012). These objects present very low eccentricities (less than 0.01) and their rotations appear to be synchronous, although there is no confirmation yet (Tiscareno et al. 2009).

Tidal dissipation slowly modifies the rotation rate of close-in planets and satellites (e.g., MacDonald 1964; Correia 2009). For rigid bodies, when the rotation rate and the mean motion have the same magnitude, the dissipative tidal torque may be counterbalanced by the conservative torque due to the axial asymmetry of the inertia ellipsoid. For eccentric orbits, this conservative torque allows for the capture of the spin rate in a half-integer commensurability with the mean motion, usually called spin–orbit resonance (Colombo 1965; Goldreich & Peale 1966; Correia & Laskar 2009). In addition, for very eccentric orbits or large axial asymmetries, the rotational libration width of the individual resonances may overlap, and the rotation becomes chaotic (Wisdom et al. 1984; Wisdom 1987). However, for nearly circular orbits, the only possibility for the spin is the synchronous resonance (e.g., Goldreich & Peale 1966; Correia & Laskar 2009). Since tidal dissipation simultaneously damps the eccentricity to zero (e.g., Hut 1980; Correia 2009), all the main satellites in the solar system are observed in quasi-circular orbits and synchronous rotation.

Contrarily to the classical two-body problem, where circular orbits are unperturbed, in the case of coorbital bodies, the orbits often present long-term librations around the Lagrange equilibrium points. As a consequence, there is a permanent misalignment of the rotating body long inertia axis from the radius vector to the central body (Figure 1). The resulting torque on the rotating body's figure induces some rotational libration (Tiscareno et al. 2009; Robutel et al. 2011, 2012). The combination of both libration motions (orbital and rotational) may give rise to some unexpected behaviors for the rotation rate. In this paper, we investigate all the possibilities for the final rotation of coorbital bodies in quasi-circular orbits.

2. MODEL

Let us denote m_0 the mass of the central body, m the mass of the rotating body, and m_c the mass of the coorbital companion (Figure 1). We adopt here the theory developed by Érdi (1977) adapted to the planetary problem (Robutel et al. 2012), and limited to the first order in $\mu = (m + m_c)/(m_0 + m + m_c)$. We additionally assume quasi-circular orbits (negligible eccentricity) with average radius r_0 for both coorbital bodies. The polar coordinates (r, f) for m centered on m_0 are given by (Robutel et al. 2012):

$$r = r_0 \left(1 - \frac{2\delta}{3n}\dot{\zeta}\right), \tag{1}$$

$$f = \delta\zeta + nt + f_0, \tag{2}$$

$$\ddot{\zeta} = -3\mu n^2 [1 - (2 - 2\cos\zeta)^{-3/2}] \sin\zeta, \tag{3}$$

where n is the orbital mean motion, $\delta = m_c/(m + m_c)$, and f_0 is a constant. The system can be stable as long as $\mu < 0.03812$ (Gascheau 1843; Siegel & Moser 1971).

[3] http://www.minorplanetcenter.net/

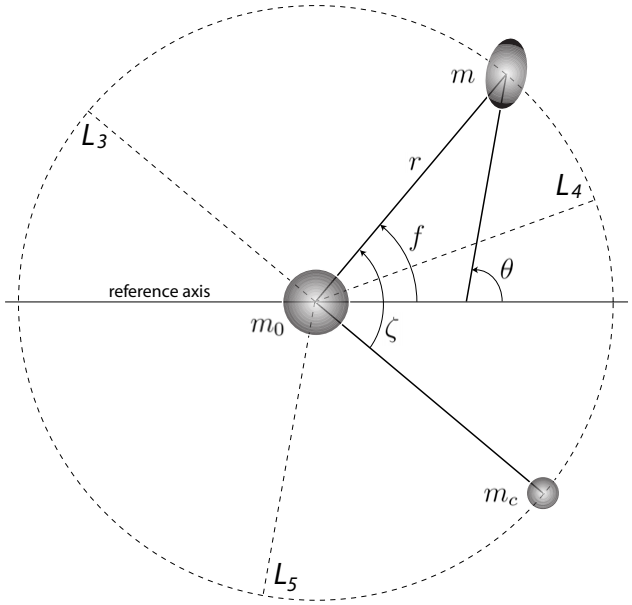

Figure 1. Reference angles for the coorbital system. m_0 is the mass of the central body, m the mass of the rotating body, and m_c the mass of the coorbital companion. θ is the rotation angle of m, r its distance to the central body, and f its true anomaly. ζ is the angle between the directions of m_c and m.

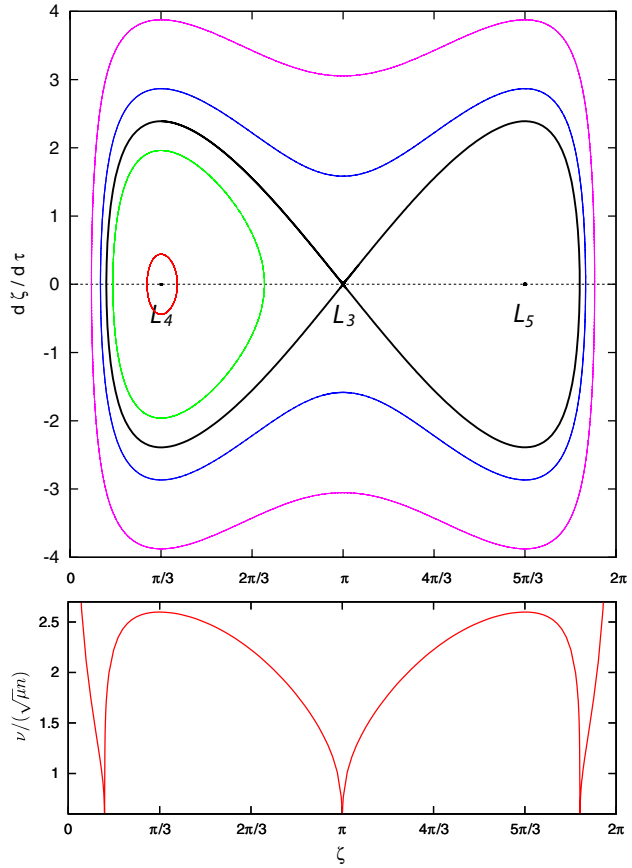

Figure 2. Longitudinal variations of coorbital bodies (Equation (14)) in the plane $(\zeta, d\zeta/d\tau)$ (top), and orbital libration frequency taken over the dashed line (ν vs. ζ with $d\zeta/d\tau = 0$) (bottom). The black curve is the separatrix between the tadpole and the horseshoes orbits ($\zeta_{\min} \approx 24°$). The two tadpole orbits surrounding L_4 correspond to $\alpha = 10°$ and $\alpha = 50°$, while the two horseshoe orbits are associated to $\alpha = 160°$ and $\alpha = 166°$.

(A color version of this figure is available in the online journal.)

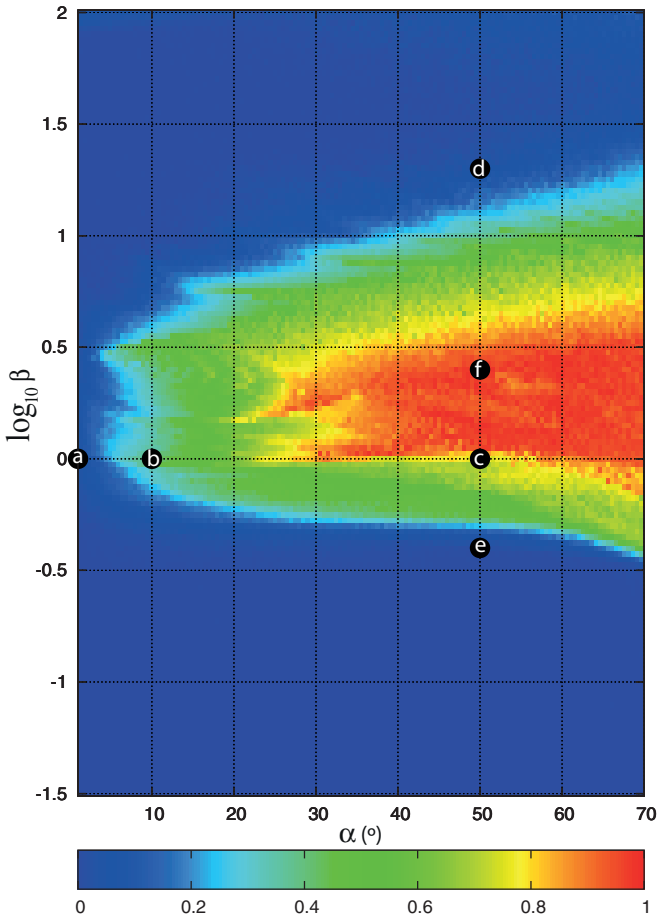

Figure 3. Stability analysis of the rotation rate close to the synchronization for $(\alpha, \log_{10}\beta) \in [0° : 70°] \times [-1.5 : 2]$ (tadpole orbits). The color index indicates the proportion of chaotic orbits inside the studied domain: from dark blue for fully regular to red for entirely chaotic. Above the chaotic region ($\log_{10}\beta > 0$) only synchronous rotation is possible, while below it ($\log_{10}\beta < 0$) several spin–orbit resonances are possible. In this plot we fixed $\mu \simeq m_c/m_0 = 10^{-3}$ and $m/m_c = 10^{-3}$, but these values do not significantly affect the results as long as $m/m_c < 0.1$ (Figure 6). The black circles correspond to the locations of the six examples presented in Figures 4 and 5.

(A color version of this figure is available in the online journal.)

Equation (3) governs the relative angular position of the coorbitals. Its solutions, plotted in Figure 2, are periodic with an associated frequency ν of the order of $\sqrt{\mu}n$ (Érdi 1977). There are stable equilibria, L_4 and L_5, for $(\zeta_0, \dot{\zeta}_0) = (\pm\pi/3, 0)$, and unstable equilibrium, L_3, for $(\zeta_0, \dot{\zeta}_0) = (\pi, 0)$. The trajectories starting with initial conditions $\zeta_0 = \pm\pi/3$, $|\dot{\zeta}_0| < n\sqrt{6\mu}$ describe tadpole orbits around L_4 or L_5, and those starting from $\zeta_0 = \pm\pi/3$, $|\dot{\zeta}_0| > n\sqrt{6\mu}$ evolve on horseshoe orbits (Figure 2). The separatrix between these two types of orbits is given by $\zeta_{\min} \approx 24°$ (for more details see Robutel et al. 2012).

The amplitude of the radial variations is usually very small, so that the orbit remains nearly circular (Equation (1)), but the longitudinal half-maximal libration amplitude,

$$\alpha \equiv |\zeta_{\max} - \zeta_{\min}|/2$$

can be very large, depending on the initial conditions (Figure 2).

Let us denote $A < B < C$ the moments of inertia of the rotating body. The equation of motion for the rotation angle, θ,

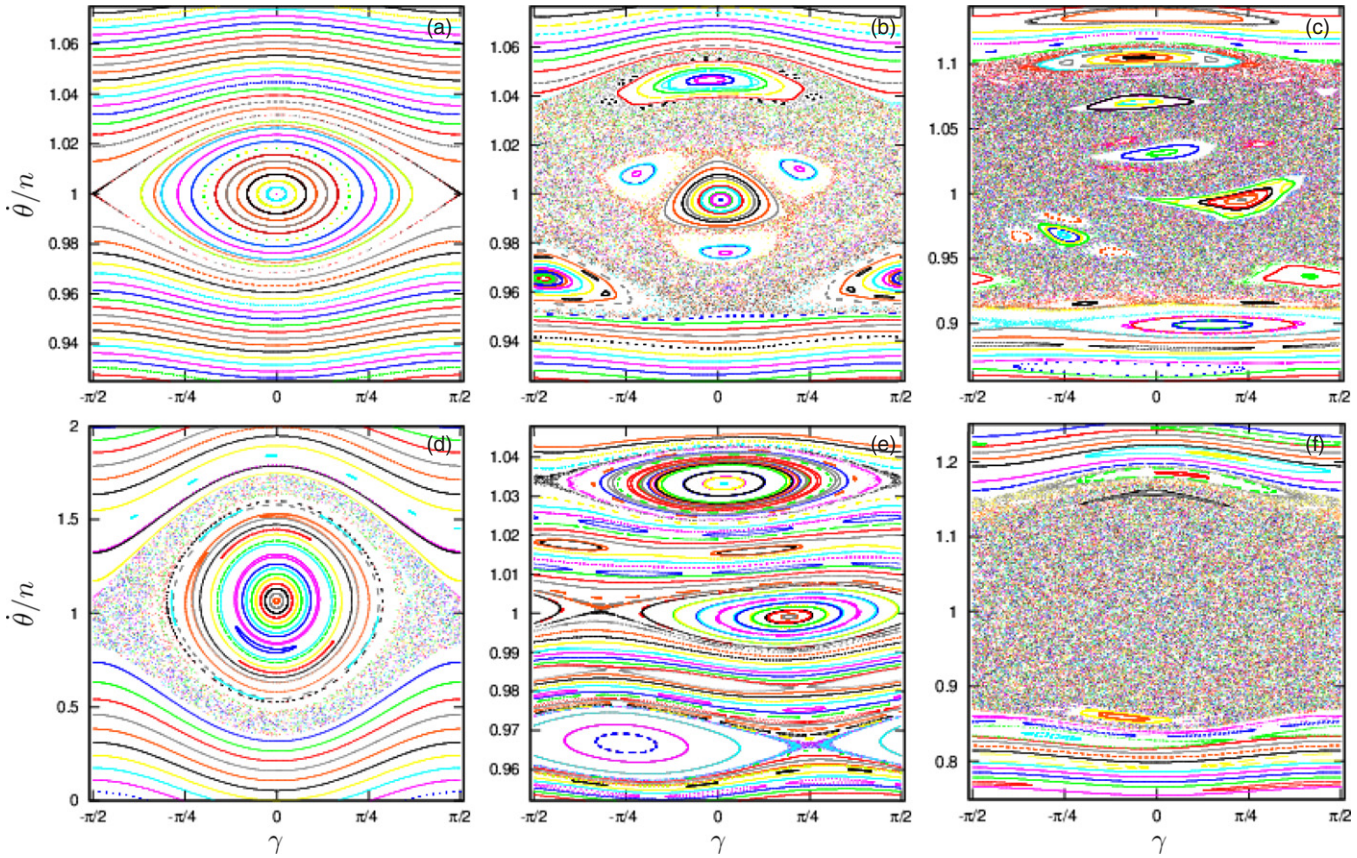

Figure 4. Poincaré surface sections in the plane $(\gamma, \dot{\theta}/n)$ deduced from the time–$2\pi/\nu$ map of the flow (Equation (4)). The angle γ is reduced modulo π. In the top graphs we fix $\beta = 1$ and increase the amplitude α: (a) $\alpha = 0°$. In this case, the dynamics is the same as a simple pendulum for all β; (b) $\alpha = 10°$. Although the super and sub-synchronous islands are small (Equation (10)), the partial overlap of the resonances already generate a significant chaotic region; (c) $\alpha = 50°$. For large amplitudes, the islands' overlap give rise to a huge unstable region surrounding the synchronization. In the bottom graphs we fix $\alpha = 50°$ and vary β: (d) $\beta = 10^{1.3}$. The three islands merged generating a chaotic layer in the neighborhood of the synchronization separatrix, as for the modulated pendulum; (e) $\beta = 10^{-0.4}$. The three main resonant islands are isolated, narrow chaotic regions are present along the associated separatrices; (f) $\beta = 10^{0.4}$. Deep inside the chaotic zone, in this case no stable motion is possible.

(A color version of this figure is available in the online journal.)

is then given by (e.g., Murray & Dermott 1999):

$$\ddot{\gamma} = -\frac{\sigma^2}{2}\left(\frac{r_0}{r}\right)^3 \sin 2(\gamma - \delta(\zeta - \zeta_0)), \tag{4}$$

where

$$\gamma = \theta - nt - f_0 - \delta\zeta_0, \tag{5}$$

and

$$\sigma = n\sqrt{3\frac{B-A}{C}}, \tag{6}$$

which is approximately the frequency for small-amplitude rotational librations.

For the tidal dissipation we adopt a viscous linear model, whose contribution to the rotation is given by (Mignard 1979; Correia & Laskar 2004):

$$\ddot{\gamma} = -K\left(\frac{r_0}{r}\right)^6 (\dot{\gamma} - \delta\dot{\zeta}), \tag{7}$$

where

$$K = 3n\frac{k_2}{\xi Q}\left(\frac{R}{r_0}\right)^3\left(\frac{m_0}{m}\right) \tag{8}$$

is a dissipation constant, with k_2 the second Love number, $Q^{-1} \equiv n\Delta t$ the dissipation factor, Δt the dissipation time lag, R the radius of the rotating body, and ξ its normalized moment of inertia.

3. DYNAMICAL ANALYSIS

For small-amplitude orbital librations ($\alpha \ll 1$), a simple linear theory can be used to understand the diversity of rotational behaviors. In this case, the solution of Equation (3) is given by (Érdi 1977)

$$\zeta = \zeta_0 + \alpha \sin(\nu t), \tag{9}$$

where $\nu \approx n\sqrt{27\mu}/2$. At first order in α, expression (4) simplifies as:

$$\ddot{\gamma} = -\frac{\sigma^2}{2}\left[\sin 2\gamma + \alpha^+ \sin 2\left(\gamma - \frac{\nu}{2}t\right) - \alpha^- \sin 2\left(\gamma + \frac{\nu}{2}t\right)\right], \tag{10}$$

where $\alpha^\pm = \alpha(1 \pm \nu/n)\delta$. We then have three main islands of rotational libration, $\dot{\gamma} = \dot{\theta} - n = 0, \pm\nu/2$, with half-widths σ and $\sigma\sqrt{\alpha^\pm}$, respectively. For $\mu \ll 1$ and $m \ll m_c$, we get $\alpha^\pm = \alpha$. Therefore, together with the classical synchronous equilibrium at $\dot{\theta} = n$, there exists two additional possibilities for the spin at the super- and sub-synchronous resonances $\dot{\theta} = n \pm \nu/2$.

More generally, since ζ is a periodic function with frequency ν, we can write (Robutel et al. 2011):

$$\left(\frac{r_0}{r}\right)^3 e^{-\mathrm{i}2\delta\zeta} = \sum_{k\in\mathbb{Z}} \rho_k e^{\mathrm{i}(k\nu t + \phi_k)}, \tag{11}$$

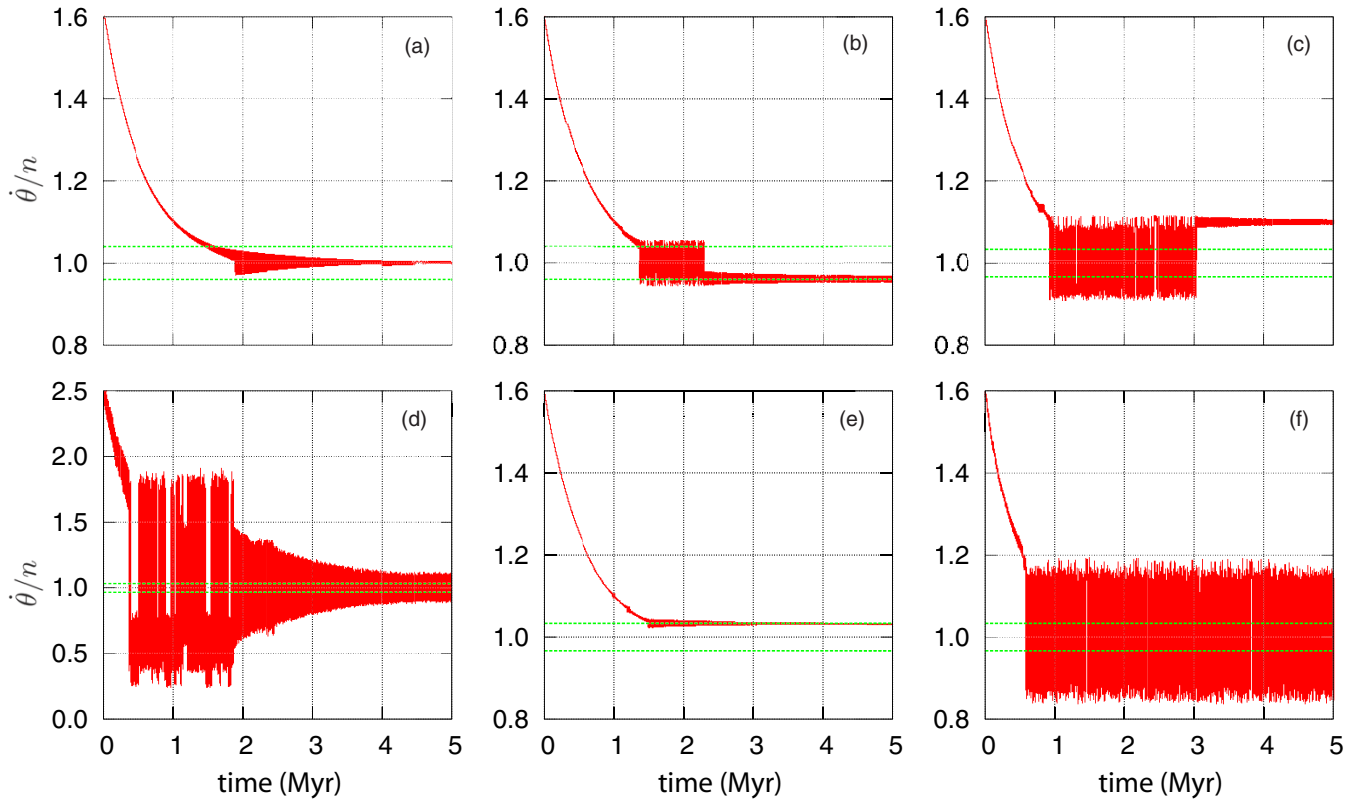

Figure 5. Examples of the final evolution of the rotation of a coorbital body. We numerically integrate the Equations (1)–(4) with $n = 17.78$ yr^{-1} (corresponding to $m_0 = 1\ M_\odot$ and $r_0 = 0.5$ AU), together with tidal dissipation using $K = 250$ yr^{-1} (Equation (7)). We show an example for each pair (α, β) taken from Figure 4. The initial rotation rate is $\dot{\theta}/n = 2.5$ in (d) and $\dot{\theta}/n = 1.6$ in all the other plots. The green dotted lines give the position of the super- and sub-synchronous resonances $n \pm \nu/2$ (Equation (10)).

(A color version of this figure is available in the online journal.)

where ρ_k and ϕ_k are the amplitude and the phase shift of each harmonic, that depend on α. Thus, expression (4) becomes:

$$\ddot{\gamma} = -\frac{\sigma^2}{2} \sum_{k\in\mathbb{Z}} \rho_k \sin(2\gamma + k\nu t + \phi_k), \tag{12}$$

where the main resonances can be found for $\dot{\theta} = n \pm k\nu/2$, k being an integer.

The general problem for the spin–orbit evolution of quasi-circular coorbital bodies is reduced to the analysis of the two frequencies, ν and σ, and the amplitude α. However, by rescaling the time using $\tau = \sqrt{\mu} n t$, we can rewrite Equations (1), (3) and (4) as

$$r = r_0 \left(1 - \sqrt{\mu}\frac{2\delta}{3}\frac{d\zeta}{d\tau}\right) \simeq r_0, \tag{13}$$

$$\frac{d^2\zeta}{d\tau^2} = -3[1 - (2 - 2\cos\zeta)^{-3/2}] \sin\zeta, \tag{14}$$

$$\frac{d^2\gamma}{d\tau^2} = -\frac{\beta^2}{2}\left(\frac{r_0}{r}\right)^3 \sin 2(\gamma - \delta(\zeta - \zeta_0)), \tag{15}$$

with

$$\beta \equiv \sigma/(\sqrt{\mu} n) \sim \sigma/\nu.$$

We see that the orbital motion is almost independent of μ, since $\mu < 0.038$, and that the rotational motion only depends on β. The global dynamics of the spin is then approximately controlled by only two parameters: α and β.

We can perform a stability analysis of $\dot{\gamma}$ in the plane (α, β) to quickly identify the rotational regime for any system of coorbital bodies that is near the synchronous equilibrium. If isolated, the half-width of the synchronous resonant island in the direction of $d\gamma/d\tau$ is equal to β. Thus, for a given (α, β) we select 400 equi-spaced values of $d\gamma/d\tau$ in the interval $[-2\beta : 2\beta]$ and fix the initial value of γ at the synchronization libration center. The corresponding solutions are integrated using the Equations (13)–(15) and their dynamical nature (stable/unstable) is deduced from frequency analysis (Laskar 1990, 1993), which gives the fraction of chaotic trajectories.

In Figure 3 we show the results for tadpole orbits with $\mu \simeq m_c/m_0 = 10^{-3}$ and $m/m_c = 10^{-3}$ (for instance, an Earth-like planet around a Sun-like star with a Jupiter-like coorbital). The color index indicates the proportion of chaotic orbits inside the studied domain: from dark blue for fully regular to red for entirely chaotic. Depending on the α and β values, the rotation can present a wide variety of behaviors, ranging from non-synchronous equilibria to chaotic motion. A common way of visualizing and understanding the different regimes is to use Poincaré surface sections (e.g., Wisdom 1987; Morbidelli 2002). Therefore, we selected a few representative pairs (α, β) and plotted the corresponding diagrams in Figure 4.

For $\alpha = 0$, the coorbital is at equilibrium at a Lagrangian point. In this particular case, the orbital motion is the same as on an unperturbed circular orbit, so the only possibility for the spin is the synchronous rotation (Figure 4(a)). For non-zero amplitude orbital librations α, the equation for the rotation of the body (Equation (4)) can be decomposed in a series of individual resonant terms with frequencies $n \pm k\nu/2$

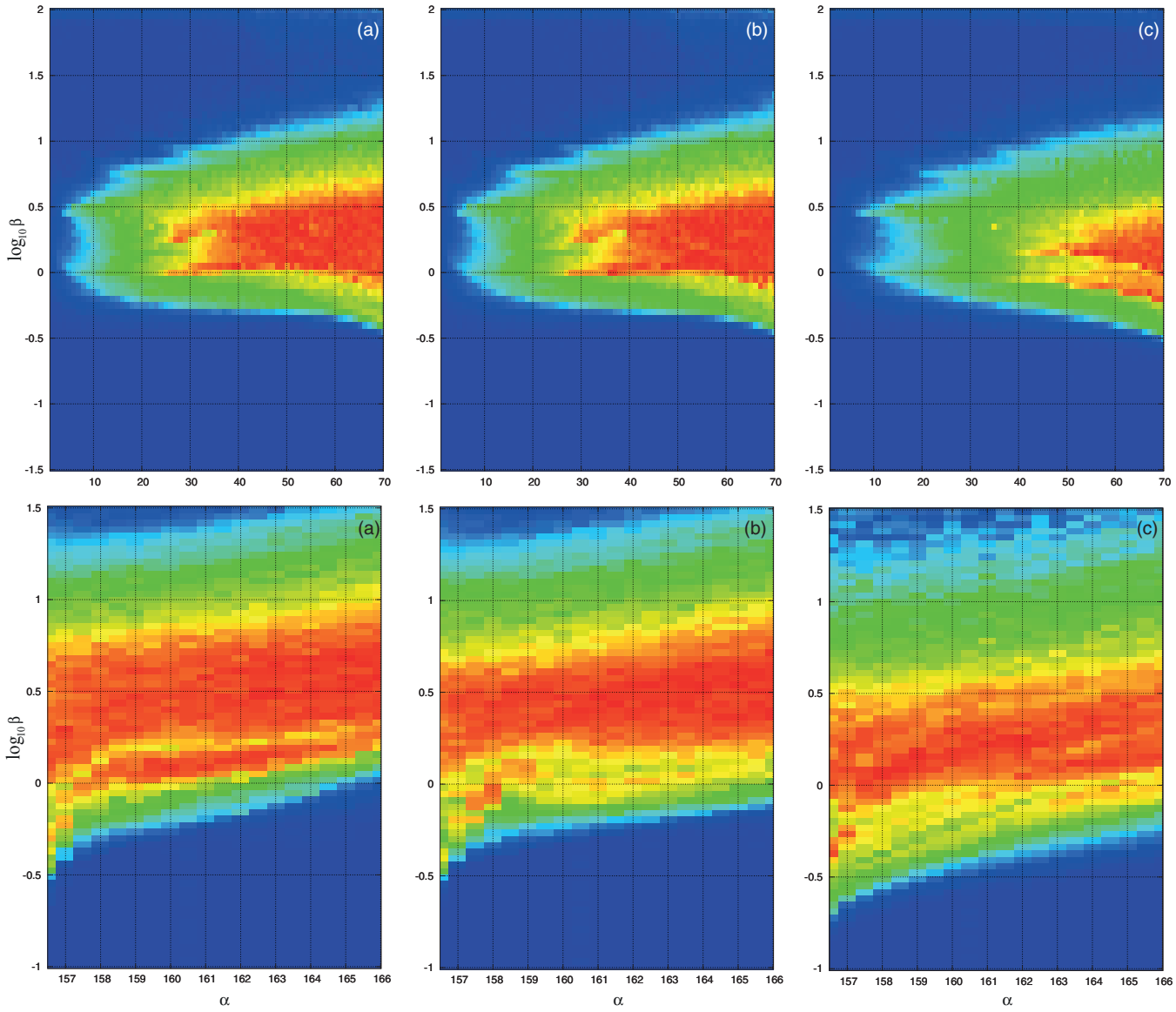

Figure 6. Same plots as in Figure 3 ($m/m_c = m_c/m_0 = 10^{-3}$), but for different mass ratios. Top pictures correspond to tadpole-type orbits $(\alpha, \log_{10}\beta) \in [0^\circ : 70^\circ] \times [-1.5 : 2]$, while bottom pictures correspond to horseshoe type orbits $(\alpha, \log_{10}\beta) \in [156^\circ : 166^\circ] \times [-1 : 1.5]$. We fix $m_c/m_0 = 10^{-6}$ and vary m/m_c: (a) $m/m_c = 10^{-3}$ ($\delta = 0.999$); (b) $m/m_c = 0.1$ ($\delta = 10/11$); (c) $m/m_c = 1$ ($\delta = 1/2$).

(A color version of this figure is available in the online journal.)

(at first order), where k is an integer (Equation (12)). Each term individually behaves like a pendulum, where the rotation can be trapped. The amplitude of each term increases with α. For small-amplitude orbital librations ($\alpha \ll 1$) only the first three terms $k = 0, \pm 1$ are important (Equation (10)). As α increases, additional spin–orbit equilibria appear and extended chaotic regions are possible for the spin.

For $\beta \ll 1$, the resonant islands are well separated apart (Figure 4(e)). Thus, the rotation can be captured in individual spin–orbit resonances and stay there. In the linear approximation (Equation (10)), for rotation rates decreasing from higher values, the super-synchronous resonance $\dot{\theta} = n + \nu/2$ is the most likely possibility (Figure 5(e)). Synchronous rotation is also possible, if the rotation escapes capture in the previous resonance. For rotation rates increasing from lower values, the sub-synchronous resonance $\dot{\theta} = n - \nu/2$ is encountered first. For large-amplitude orbital librations, capture in stable higher order spin–orbit resonances is also possible.

When $\beta \sim 1$, some individual resonant islands overlap. Analyzed separately, rotational libration could be expected in neighboring resonances, but such behavior is not possible and the result is chaotic rotation (Chirikov 1979; Morbidelli 2002; Figure 4(f)). This means that the rotation exhibits random variations in short periods of time. For moderate chaos, the chaotic region may provide a path into the sub-synchronous resonance (Figure 5(b)), or to initially escaped higher-order resonances (Figure 5(c)). In the linear approximation (Equation (10)), the chaos is confined within the super- and sub-synchronous resonances ($|\dot{\theta} - n| \lesssim \sigma(1 + 2\sqrt{\alpha})$) (Figure 4(b)), but for larger orbital libration amplitudes, the chaotic regions can be extended (Figure 4(c) and Figure 6).

For $\beta \gg 1$, the resonances come closer, and all individual rotational libration widths embrace the synchronous equilibrium.

At this stage, chaotic rotation can still be observed around the separatrix of the synchronous resonance, but the motion is regular nearer the center (Figure 4(d)). Therefore, when the rotation of a body is decreasing by tidal effect, the rotation will be shortly chaotic during the separatrix transition, but it is ultimately stabilized in the synchronous resonance (Figure 5(d)), as if the body evolved in a unperturbed circular orbit (Figure 5(a)).

4. DISCUSSION

In order to test the reliability of the dynamical picture described in the previous section, we have numerically integrated the Equations (1)–(4) together with tidal dissipation (Equation (7)) using $K = 250\ \mathrm{yr}^{-1}$. Dissipation is set to a high value so that we can speed-up the simulations. However, lower K values have no impact in the capture scenario (e.g., Henrard 1982), and the evolution time-scale is roughly proportional to K^{-1}. In Figure 5 we show an example for each pair (α, β) taken from Figure 4. The initial rotation rate is $\dot{\theta}/n = 2.5$ in Figure 5(d) and $\dot{\theta}/n = 1.6$ in all the other plots. The green dotted lines give the position of the super- and sub-synchronous resonances $n \pm \nu/2$ (Equation (10)). It is interesting to observe that the sub-synchronous resonance can be reached after some wandering in the chaotic zone (Figure 5(b)). Capture in higher order spin–orbit resonances can also occur (Figure 5(c)).

Slightly different initial conditions may lead to totally different final equilibrium configurations. Different tidal models can also change the individual capture probabilities in resonance (Goldreich & Peale 1966), but not the global picture described in this paper. Instead of using the simplified Equations (1)–(3), we also run some simulations integrating direct n-body equations for the orbital motion, but no differences were observed.

We can also test the robustness of the stability analysis diagram shown in Figure 3 for different mass ratios. In Figure 6 we then fix $m_c/m_0 = 10^{-6}$ and vary m/m_c, instead of using $m/m_c = m_c/m_0 = 10^{-3}$ (Figure 3). We confirm that the impact of $\mu \simeq m_c/m_0$ in the global analysis of the spin is imperceptible (Figures 6(a) and (b)). However, for comparable coorbital masses ($m/m_c > 0.1$) the chaotic region shrinks (Figure 6(c)), because the resonance width is proportional to $\delta = m_c/(m+m_c)$ (Equation (10)). For identical coorbital masses ($m = m_c$) the orbital libration amplitude is reduced by one-half, so there is less overlap between neighbor spin–orbit resonances.

In Figure 6 we simultaneously plot the stability analysis for tadpole-type orbits (top) and horseshoe-type orbits (bottom). We observe that for horseshoe orbits the same rotational regimes as for tadpole orbits are still present. However, the chaotic regions are more extended, since the orbital libration amplitude is larger $\alpha \in [156^\circ : 166^\circ]$. Therefore, more harmonics to the expansion of the rotational torque must be taken into account (Equation (12)), increasing the number of relevant spin–orbit resonances and the superposition between them.

In the stability analysis diagrams, $\beta \gg 1$ corresponds to large rotational libration widths and/or small mass-ratios (Equation (15)). This is exactly the situation for all Saturn's coorbital satellites, due to their prominent ellipsoidal figures ($\sigma/n \sim 1$) and tiny mass-ratios ($\mu < 10^{-6}$; Robutel et al. 2012). As a consequence, the only possibility for these satellites is the synchronous resonance. However, for close-in exoplanets one can expect smaller axial asymmetries and larger mass-ratios (Laughlin & Chambers 2002; Beaugé et al. 2007; Cresswell & Nelson 2009; Giuppone et al. 2010), that is, smaller β values. For Earth-like planets ($m/m_0 \sim 10^{-6}$), we have $\sigma/n \sim 10^{-3}$ (Yoder 1995) which gives $\beta \sim 10^{-1}$ for a Jupiter-like coorbital ($\mu \sim 10^{-3}$), and $\beta \sim 1$ for another Earth-like coorbital ($\mu \sim 10^{-6}$), respectively. Thus, Earth-like planets may present non-synchronous or chaotic rotation (Figure 5), an important point to take into account in future orbital evolution studies (e.g., Rodríguez et al. 2013), and habitability studies (e.g., Selsis et al. 2007).

The present work should apply more generally to coorbital bodies in eccentric orbits, for which the classic spin–orbit resonances (Colombo 1965; Goldreich & Peale 1966; Correia & Laskar 2009) will split into several components $(k_1 n \pm k_2 \nu)/2$, where k_1 and k_2 are integers. It should also apply to other orbital resonant configurations, in particular for low order mean-motion resonances.

We acknowledge support by PICS05998 France–Portugal program, and Fundação para a Ciência e a Tecnologia, Portugal (PEst-C/CTM/LA0025/2011).

REFERENCES

Beaugé, C., Sándor, Z., Érdi, B., & Süli, Á. 2007, A&A, 463, 359
Chirikov, B. V. 1979, PhR, 52, 263
Colombo, G. 1965, Natur, 208, 575
Correia, A. C. M. 2009, ApJL, 704, L1
Correia, A. C. M., & Laskar, J. 2004, Natur, 429, 848
Correia, A. C. M., & Laskar, J. 2009, Icar, 201, 1
Cresswell, P., & Nelson, R. P. 2009, A&A, 493, 1141
Érdi, B. 1977, CeMec, 15, 367
Gascheau, G. 1843, C. R. Acad. Sci. Paris, 16, 393
Giuppone, C. A., Beaugé, C., Michtchenko, T. A., & Ferraz-Mello, S. 2010, MNRAS, 407, 390
Goldreich, P., & Peale, S. 1966, AJ, 71, 425
Henrard, J. 1982, CeMec, 27, 3
Hut, P. 1980, A&A, 92, 167
Lagrange, J. J. 1772, Œuvres Complètes VI, 272 (Paris: Gauthier-Villars), (1869)
Laskar, J. 1990, Icar, 88, 266
Laskar, J. 1993, PhyD, 67, 257
Laughlin, G., & Chambers, J. E. 2002, AJ, 124, 592
MacDonald, G. J. F. 1964, RvGeo, 2, 467
Mignard, F. 1979, M&P, 20, 301
Morbidelli, A. 2002, Modern Celestial Mechanics: Aspects of Solar System Dynamics (London: Taylor and Francis)
Murray, C. D., & Dermott, S. F. 1999, Solar System Dynamics (Cambridge: Cambridge Univ. Press)
Robutel, P., Rambaux, N., & Castillo-Rogez, J. 2011, Icar, 211, 758
Robutel, P., Rambaux, N., & El Moutamid, M. 2012, CeMDA, 113, 1
Rodríguez, A., Giuppone, C. A., & Michtchenko, T. A. 2013, CeMDA, 117, 59
Selsis, F., Kasting, J., Levrard, B., et al. 2007, A&A, 476, 1373
Siegel, C. L., & Moser, J. 1971, Lectures on Celestial Mechanics (Berlin: Springer), 13
Tiscareno, M. S., Thomas, P. C., & Burns, J. A. 2009, Icar, 204, 254
Wisdom, J. 1987, AJ, 94, 1350
Wisdom, J., Peale, S. J., & Mignard, F. 1984, Icar, 58, 137
Wolf, M. 1906, AN, 170, 353
Yoder, C. F. 1995, in Global Earth Physics: A Handbook of Physical Constants, ed. T. J. Ahrens (Washington, DC: American Geophysical Union), 1